Friction **10**(5): 706–716 (2022)
https://doi.org/10.1007/s40544-020-0484-y
ISSN 2223-7690
CN 10-1237/TH
RESEARCH ARTICLE

Structure, tribological properties, and the growth mechanism of *in-situ* generated TiC in titanium cermet

Xiaolei SUN[1], Yong LUO[1,2,4,6,*], Junyang WANG[4], Qingliang WANG[4], Jianghao QIAO[4], Andrew BEADLING[5], Michael BRYANT[5], Zhongmin JIN[3]

[1] *School of Chemical Engineering&Technology, China University of Mining and Technology, Xuzhou 221116, China*

[2] *State Key Laboratory of Solid Lubrication, Lanzhou Institute of Chemical Physics, Chinese Academy of Sciences, Lanzhou 730000, China*

[3] *School of Mechanical Engineering, Southwest Jiaotong University, Chengdu 610031, China*

[4] *School of Materials Science and Physics, China University of Mining and Technology, Xuzhou 221116, China*

[5] *School of Mechanical Engineering, University of Leeds, Leeds LS2 9JT, UK*

[6] *State Key Laboratory of Tribology, Tsinghua University, Beijing 100084, China*

Received: 27 July 2020 / Revised: 30 September 2020 / Accepted: 30 December 2020

Abstract: Titanium cermet combining metallic toughness with ceramic wear resistance has been proven to be a potential candidate for implanted joint material. In this work, titanium cermet was synthesized by means of the elevated temperature solid carburizing technology. The $Ti_{13}Nb_{13}Zr$ alloy surface was found to be converted into TiC ceramic layer combined with a carbon strengthened diffusion zone underneath. The overall thickness of the carburized region grew to about 100 μm after 120 min carburization at 1,500 K. In order to clarify the growth behaviors of TiC ceramic layer, a growth mechanism is proposed. At the beginning of carburizing process, carbonaceous gas decomposed from carburizer due to high temperature and then converted to free atomic carbons through reduction reaction. Then, *in-situ* generated TiC ceramic layer possessing certain thickness formed on the surface, meanwhile, the inner carbon diffusion zone also grew inwards due to physical diffusion of carbon, and finally forming a gradient carbon distribution. In addition, the tribological behaviors of the new materials were evaluated through reciprocating ball-on-plate sliding wear tests in bovine calf serum. Although there was an increase in friction coefficient, the wear rate decreased by 59.6% due to the formation of the wear-resistant TiC ceramic layer. The wear mechanisms evolved from severe abrasive wear for bare $Ti_{13}Nb_{13}Zr$ alloy to mild adhesive wear for titanium cermet.

Keywords: titanium cermet; growth mechanism; wear mechanism

1 Introduction

Total hip arthroplasty (THA) surgery is one of the most successful operations for patients suffered from degenerative joints diseases [1, 2]. With the advances in prosthesis design and manufacture, the success rate of THA has been increased significantly. Nowadays, not only the aged, but the young patients with more active life styles are also prone to THA. Since articulating surfaces have to undergo dynamic loading, multi-directional sliding friction, and severe tribo-corrosion for a long time, the wear is inevitable in in-vivo. Up to now numerous postoperative complications have been confirmed to be related to the accumulative wear debris and cytotoxic metal ions, especially for traditional materials such as CoCrMo alloy and stainless steel [3, 4]. By contrast, medical titanium alloys exhibit beneficial mechanical properties and outstanding corrosion resistance, which render them the competitive candidates for implanted joint materials [5].

* Corresponding author: Yong LUO, E-mail: sulyflying@cumt.edu.cn

Unfortunately, most titanium alloys have poor tribological properties due to low resistance to plastic shearing and mechanical instability of metal oxide layer, especially when applying to the multi-directional sliding condition. For this, lots of surface treatment methods such as ion implantation, physical vapor deposition (PVD), chemical vapor deposition (CVD), micro arc oxidation (MAO), and plasma spraying have been employed to overcome this difficulty [6–8]. Among them, carburization is believed to be a practicable approach to provide excellent wear resistance for titanium alloy. Our previous work has revealed that hard TiC ceramic layers with gradient microstructure were successfully synthesized on titanium alloys surfaces through carburization [9]. The carburized titanium alloy was designated as titanium cermet, and successfully prepared for the femoral head for the first time [10].

Although the mechanical properties and wettability have been investigated systematically [11, 12], the growth mechanism and wear mechanisms of titanium cermet were still not clear, which hindered the widely clinical application of titanium cermet. Thus, it is of great significance to explore the growth mechanism and underlying wear mechanisms of titanium cermet, it will be of help towards the development of high-performance titanium cermet artificial joint.

2 Materials and methods

2.1 Materials and sample preparation

Most of our previous investigations about titanium cermet were based on Ti_6Al_4V alloy containing cytotoxic elements such as Al and V, which may damage the nervous system once released inside the human body [4, 13]. In addition, Ti_6Al_4V alloy has much higher elastic modulus than cortical bone, which will prevent the needed stress being transferred to adjacent bone, resulting in bone resorption around the implant and consequently to implant loosening. At present, $Ti_{13}Nb_{13}Zr$ with better biocompatibility and lower elastic modulus has been attempted to apply to implanted joint material, but current research is still on the stage of experiment due to its poor tribological properties [14, 15]. Thus, the substrate material used for this work was biomedical β-rich $Ti_{13}Nb_{13}Zr$ alloy with the following composition in mass percent: 13.3% Nb, 13.3% Zr, and balance Ti.

$Ti_{13}Nb_{13}Zr$ alloy square samples with dimension of 15 mm × 15 mm and 5 mm in thickness were prepared by wire cutting. Samples were ground to a surface roughness of approximately Ra ~ 0.05 μm by a standard sample preparation procedure. Prior to the experiments, each sample was ultrasonically cleaned in ethanol and dried under hot air.

2.2 Elevated temperature solid carburization

Elevated temperature solid carburization (ETSC) treatment for $Ti_{13}Nb_{13}Zr$ alloy was carried out in a corundum porcelain boat put in a tube furnace (GSL-1400X, China) with Argon gas protection. The solid carburizer in use was composed of some catalyzed reagents, i.e. Na_2CO_3 (5 wt%) and $CaCO_3$ (5 wt%), and the remained charcoal. Figure 1 shows the schematic diagram of the elevated temperature solid carburization process for $Ti_{13}Nb_{13}Zr$ alloy.

It is reported that the allotropic transformation from α-Ti (hexagonal close packing structure) to β-Ti (body centered cubic structure) phase occurs in $Ti_{13}Nb_{13}Zr$ alloy when the temperature exceeds 1,008 K [16]. In general, it is easier for carbon atoms to enter body centered cubic structure rather than hexagonal

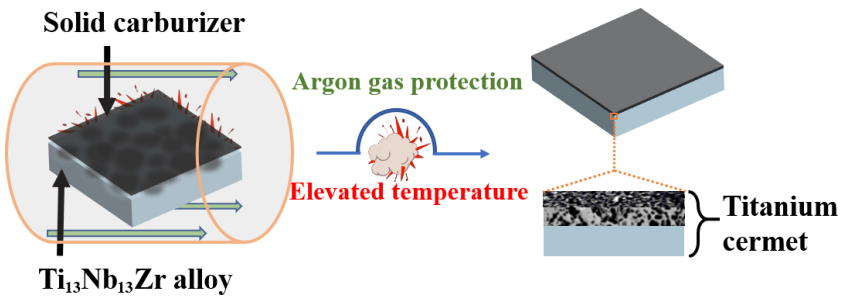

Fig. 1 Diagram of the elevated temperature solid carburization for $Ti_{13}Nb_{13}Zr$ alloy.

close packing structure. Thus, 1,500 K was selected as the carburizing temperature to ensure carburizing efficiency in this work. After packing the whole materials, $Ti_{13}Nb_{13}Zr$ alloy samples were heated up to 1,500 K and then were held for 0, 10, 30, 60, and 120 min, respectively, followed by furnace cooling to room temperature. A summary of the sample codes and carburizing parameters is given in Table 1.

2.3 Phase identification and microstructure characterization

The phase constituents of titanium cermet were examined by X-ray diffraction (XRD, D8 Advance, Bruker, Germany) with Cu radiation under 40 kV and 30 mA in the 2θ range of 20°–90°. The ETSC60 sample was cut and thinned by using a Helios G4 CX focused ion beam (FIB) miller, then the microstructure and selected area electron diffraction patterns were characterized through field emission transmission electron microscope (TEM, Tecnai F20, FEI, USA). The chemical states were identified by X-ray photoelectron spectroscopy (XPS, Axis Ultra DLD, Kratos, UK). Scanning electron microscope (SEM, SU3500, Hitachi, Japan) equipped with energy dispersive spectroscopy (EDS) was used to examine the morphologies of samples and provide an estimation of the relevant atomic percentage of elements.

2.4 Mechanical and tribological properties evaluations

The hardness of the untreated and carburized samples was measured using a Vickers hardness tester (187.5E, THBRVP, China) with the normal load of 0.98 N for 10 s. Three indentations were inserted at three different positions and the average value was taken.

Due to flexion–extension motion dominates the normal walking gait, the one-directional linearly reciprocating sliding test as a simplified articulation motion of flexion–extension was carried out to initially evaluate the tribological performance of titanium cermet, and all tests were conducted on a ball-on-plate tribometer (UMT-2, CETR, USA) under the lubrication of 25% calf serum diluted fluid. Due to the good mechanical properties [17] and superior wettability properties [18], the zirconia balls (Shanghai Unite Technology Co., Ltd.) with a diameter of 5 mm were used as the counter surfaces. The stroke length was fixed at 6 mm. The tests were run for 120 min and the frequency was 1 Hz. The normal load of 29.4 N was applied. In general, in hip implant, the contact pressure under normal gait is below 100 MPa [19], while the contact pressure in some region can reach 200 MPa under edge loading conditions [20]. In order to know the real contact state in wear tests, FUJI pressure measurement film was used to measure the actual contact pressure caused by 29.4 N, and the result showed that the actual contact pressures in most areas were about 85–102 MPa, which was consistent with the real contact pressure in hip implant. Before and after wear tests, each sample was ultrasonically cleaned in distilled water and ethanol, and then dried under hot air.

The friction coefficient was continuously recorded in the tribometer system during the test, and the loss of weight was measured by an electronic analytical scale with an accuracy of ±1 mg. Subsequently the mass loss data was converted into volume loss through the density of the alloy. Eventually, the wear rate was calculated by the changed wear volume, and the relationship between wear rate and wear volume was expressed by the following equation:

$$W = \frac{\Delta v}{F \times S} \tag{1}$$

where W is the wear rate, Δv is the volume decreased, F is the load force, and S is the sliding distance. After the wear tests, the wear tracks formed on the surfaces of samples were examined by SEM.

Table 1 Sample codes and carburizing parameters.

Sample code	Holding time (min)	Carburizing temperature (K)
ETSC0	0	1,500
ETSC10	10	1,500
ETSC30	30	1,500
ETSC60	60	1,500
ETSC120	120	1,500

3 Results and discussion

3.1 The phase identification and microstructure

XRD analysis will provide detailed information about

phase constituent evolution during the carburization. Figure 2 shows the XRD patterns of the untreated and carburized samples. It was revealed that the peak positions of the carburized samples at 35.87° (111), 41.63° (200), 60.26° (220), 72.08° (311), and 75.82° (222) belonged to TiC phase with face centered cubic (FCC) crystal structure after compared with the standard PDF Card No. 65-0966. Although the XRD patterns of all carburized samples showed similar features in peak positions, the intensities of the major TiC peaks significantly increased with the holding time, indicating the continuous TiC formation during the carburization [21]. In addition, the diffraction peaks of Nb_2O_5 (PDF Card No. 37-1468) were also noted in the XRD patterns of the carburized samples but relatively lower intensities due to the limited remaining oxygen in corundum porcelain boat. It was also worth noting that the intensities of Nb_2O_5 peaks significantly decreased with the holding time, opposite to TiC, which further confirmed the sustained TiC formation on the surface of $Ti_{13}Nb_{13}Zr$ alloy.

The typical bright field TEM image at a depth of 10 μm to the topmost surface of the ETSC60 sample is shown in Fig. 3(a). In the middle, there was an equiaxed grain about 300 nm in size with randomly distributed crystallographic orientations. Analyzing the corresponding selected area diffraction (Fig. 3(b)) pattern in the [332] direction of crystal band axis indicated it mainly composes of TiC, which was consistent with the XRD result [22]. Around the TiC grain, Ti–C solid solution zone composed of interstitial solid solution was observed due to the active carbon

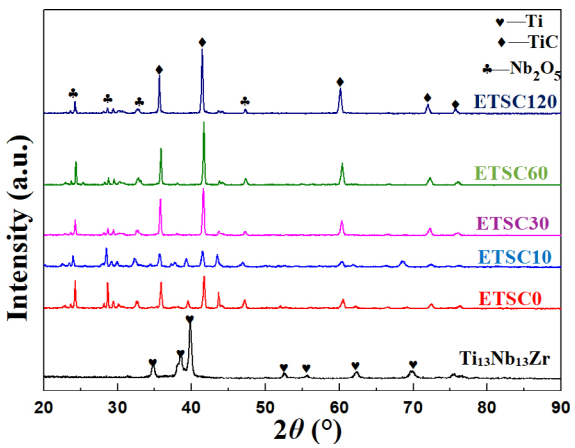

Fig. 2 XRD patterns for $Ti_{13}Nb_{13}Zr$ alloy and the carburized samples.

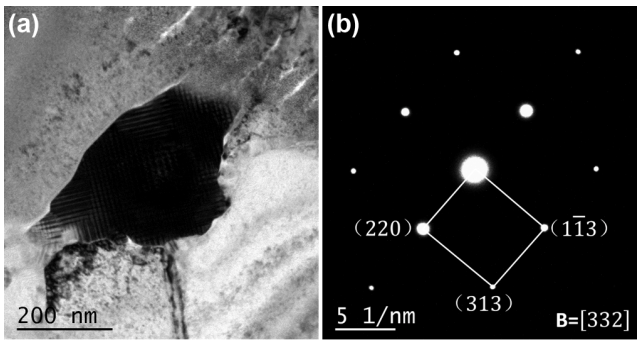

Fig. 3 (a) Bright field TEM image of ETSC60 sample and (b) the corresponding selected area electron diffraction pattern.

atoms diffusion synchronized with the reaction. In addition, it was also found that some fine cracks distributed in solid solution zone, which can be explained by the fact that the local compressive stress generated from the expanded β-Ti phase saturated by carbon atoms [23, 24]. As a result, these fine cracks were developed to release stress in solid solution zone.

The XPS peak positions as the electron binding energies for specific atomic levels were used for the identification of specimen chemical states. The C 1s peaks of 284.8 eV was used for energy calibration. As shown in Fig. 4(a), two Ti 2p peaks for ETSC60 sample were spin-orbital splitting peaks, 2p1/2 (460.8 eV) and 2p3/2 (454.7 eV), whose positions shifted to larger binging energy side compared with the corresponding peaks of pure Ti (459.8 and 453.8 eV) included in Handbook of XPS. Referring to NIST XPS database, it can be found that the binding energies of this peaks were characteristic of TiC phase. Figure 4(b) shows two peaks for the C 1s spectra. The larger C 1s peak (284.8 eV) perhaps come from the graphite formed under the elevated temperature, and the smaller one (281.3 eV) corresponded to C 1s level in TiC. These results above showed that, during the solid carburization, part of the diffused active carbon atoms reacted with titanium to form TiC phase whilst some transformed into stable graphite due to special preparation conditions [9].

As the phase constituents converted, the morphology of $Ti_{13}Nb_{13}Zr$ alloy surface also changed inevitably. The pictures displayed in Fig. 5 exhibit the microscopic examinations of carburized samples with increased holding time. It was noticed that the effect of holding

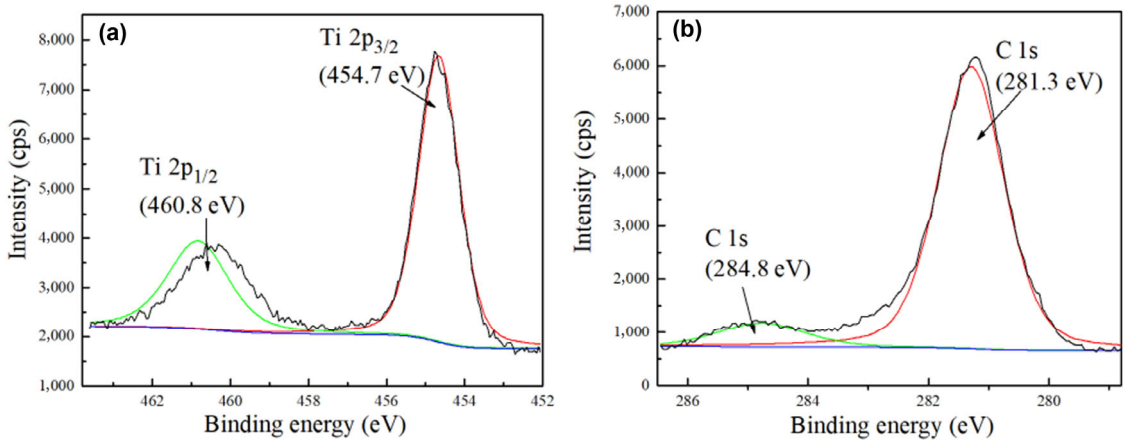

Fig. 4 XPS spectra of ETSC60 sample regarding (a) titanium and (b) carbon spectrum.

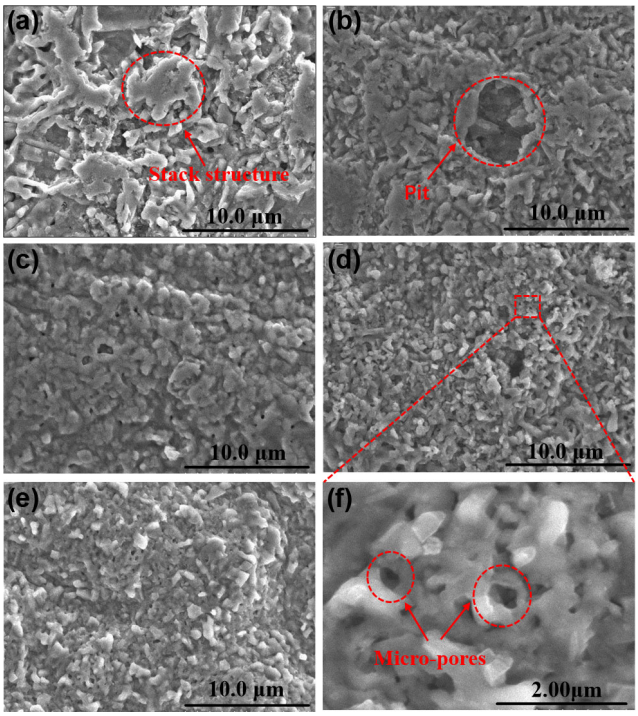

Fig. 5 Surface morphologies of the carburized samples. (a) ETSC0; (b) ETSC10; (c) ETSC30; (d) ETSC60; (e) ETSC120; and (f) magnification of 20,000-fold SEM image of sample ETSC60.

time on surface microstructure was evident. SEM observations on the surfaces of the samples subjected to short holding time, i.e. the ETSC0 and ETSC10 samples, revealed that they consisted of randomly distributed lath-structure titanium carbides and thus formed the disordered stack structure (Fig. 5(a)), which finally generated the pit shown in Fig. 5(b). When the holding time exceeded 30 min at 1,500 K, fine TiC particulates instead of lath-structure titanium carbides closely arranged on the surfaces, leading to the transition from loose to dense for ceramic layers. Figure 5(f) represents a higher magnification observation for ETSC60 sample, which provides further insight into the TiC ceramic layer. It was noticed that considerable number pores, in nano-scale, distributed on the surface and interconnected with each other, which may be explained as follows. As the carburization went on, surface carbides expanded continuously after nucleation until being squeezed between each other. In the process, thanks to the difference in orientations of the growing TiC grains, a plenty of pores with nano diameter generated, leading to the formation of the complex surface micro pore structure. For one thing, these pores facilitated the diffusion of carbon atoms inside the titanium alloy, which provided enough carbon atoms required for the growth of carburized layer. For another, micro-pores could deposit lubricants and store wear debris, therefore reducing abrasive wear. Also, it was expected to be conducive to the growth of osteoblasts and bone repair [25, 26].

3.2 The growth mechanism of TiC ceramic layer

The cross-section morphologies of the carburized samples can provide transient and intuitive information for the growth mechanism of TiC ceramic layer. Figure 6 shows the SEM cross-section image of ETSC120 sample. It was found that the carburized region was consisted of a double-layer structure with an outer TiC ceramic layer and an inner carbon diffusion zone. These two sublayers were closely interlinked to $Ti_{13}Nb_{13}Zr$ substrate mainly due to the metallurgical bonding through carburization, which provided an

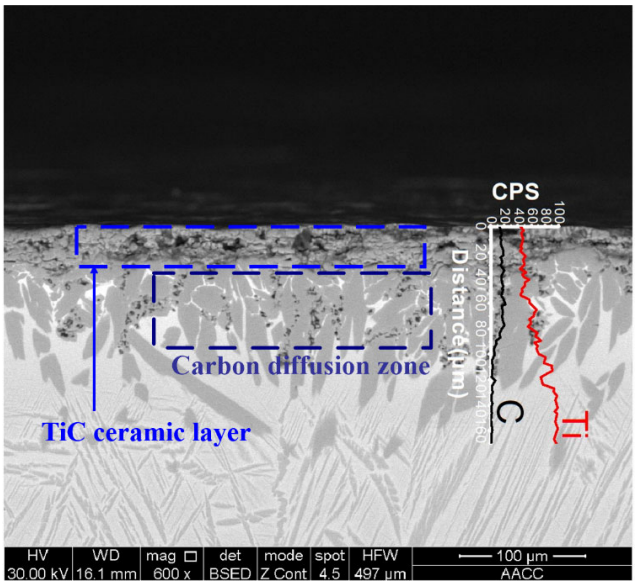

Fig. 6 The cross-section morphology of ETSC120 sample and the element distribution along the cross-section (the inset).

excellent bonding stability [27]. In contrast, the carburized region of ETSC0 and ETSC10 samples were so thin and discontinuous that they cannot covered the matrix completely, whilst two sublayers grew inwards significantly as the holding time exceeded. When the holding time increased to 120 min, the carburized region of ETSC120 sample not only exhibited relatively uniform layer but also reached to 100 μm in thickness. In addition, it was worth noting that coarse grains appeared in $Ti_{13}Nb_{13}Zr$ alloy substrate after 120 min carburization at 1,500 K. Vajpai et al. [28] considered that the increasing grain size would result in decreasing strength values and increasing ductility for $Ti_{25}Nb_{25}Zr$ alloy. In addition, it was found that fine acicular α phase precipitated within prior β grain during the cooling process, resulting in a basket-wave morphology. Chen et al. [29] believed that the fine acicular α phase was responsible for high strength but worse ductility in titanium alloy. For $Ti_{13}Nb_{13}Zr$ alloy, the effect of the elevated temperature on the grain size and mechanical properties needs to be further explored.

The EDS linear scan was conducted to explore the regularity of elemental distribution along the cross-section of titanium cermet. The scan profile (inserted in Fig. 6) perpendicular to the surface shows significant changes of Ti and C content from surface to substrate. In order to clarify the above phenomenon, the growth mechanism of TiC ceramic layer is proposed and illustrated in Fig. 7. At the beginning of carburizing process, carbonaceous gas was decomposed from carburizer for high temperature, and soon afterwards generated free atomic carbons through reduction reaction. Most carbons were absorbed by the sample surface and diffused into the substrate [21]. Then, TiC ceramic layer possessing certain thickness formed on the surface in a short term due to the sufficient carbon content. At the forefront of the extended TiC ceramic layer, the bulk of the diffused carbons atoms were consumed by the growth of TiC grains, only a few carbons atoms escaped and formed the interstitial solid solution, which finally formed a gradient carbon distribution corresponding to the evolution tendency of the EDS Linear scan profile. As the holding time extended, surface carbon concentration continued to rise. In this case, it was reported that there was more carbons diffusing in the substrate to be over the limit of single TiC phase to TiC + graphite region in Ti–C phase diagram [30], which was consistent with the XPS analysis about the presence of graphite.

3.3 Tribological properties

Hardness plays significant role in the wear of materials, and Archard's law states that the material wear mass is indirectly proportional to the material hardness. Figure 8 shows the Vickers hardness of $Ti_{13}Nb_{13}Zr$ alloy and the carburized samples. It was found that the hardness values of $Ti_{13}Nb_{13}Zr$ alloy was 226 HV. After carburization, the samples exhibited higher values attributed to the formation of hard TiC ceramic

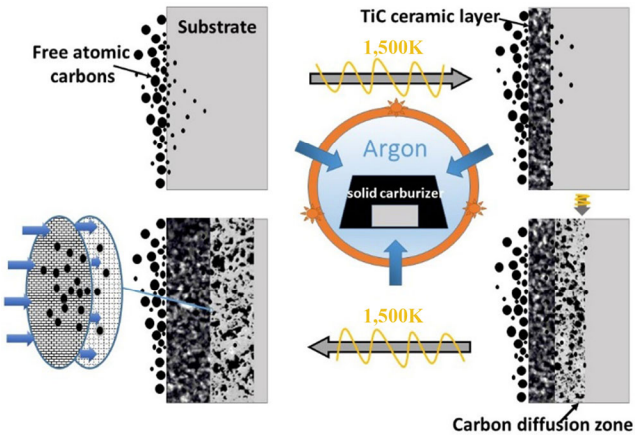

Fig. 7 The growth mechanism of TiC ceramic layer.

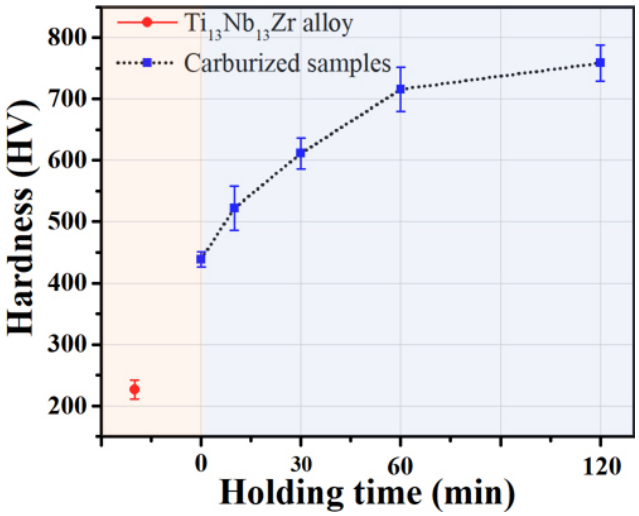

Fig. 8 Surface hardness of $Ti_{13}Nb_{13}Zr$ alloy and the carburized samples.

layer. Furthermore, as the holding time increased, the surface hardness presented a monotonic increasing trend. In particular, the hardness of ETSC120 sample with the thickest TiC layer reached to 758 HV, approximately four times higher than that of bare $Ti_{13}Nb_{13}Zr$ alloy because of the adequate growth of TiC grains after the longest holding time.

Variations of friction coefficient for $Ti_{13}Nb_{13}Zr$ alloy and the carburized samples against ZrO_2 ball under calf serum lubrication condition are shown in Fig. 9(a). Compared to the bare $Ti_{13}Nb_{13}Zr$ alloy sample, the carburized samples exhibited relatively higher values because of the coarse surface structure [31]. It was also found that all curves of the carburized samples presented similar features, an initial transient state followed by a relative steady state [32]. In the transient state, the friction coefficient values exhibited upward trend with sliding time. During the carburization, the violent chemical reaction between Ti and C caused the surface micro-pore structure, so that the topmost surface of the titanium cermet cannot achieve the good ability to resist strong mechanical forces. As a result, at the beginning of friction process, the destruction of the topmost surface ceramic layer made the contact areas increased, leading to the rise of friction coefficient. Subsequently the porous topmost surface collapsed, the stable friction occurred with relatively constant and low friction coefficient due to the compactness and tenacity of the TiC ceramic layer underneath. With the increased holding time, the carburized samples, beside sample ETSC30, exhibited lower friction coefficient attributed to the denser and flatter surface. With respect to the wear rate, it was calculated from the wear quality changes and plotted versus the holding time as illustrated in Fig. 9(b). It was found that the bare $Ti_{13}Nb_{13}Zr$ alloy sample exhibited a high wear rate of 1.36×10^{-4} $mm^3{\cdot}N^{-1}{\cdot}m^{-1}$. Then a transition was observed as ETSC0, 10, 30, 60, and 120 samples all presented significantly reduced values due to the effective protection provided by the hard TiC ceramic layer. In addition, it was obvious that the wear rates of the carburized samples decreased with the increased holding time, especially for ETSC120 sample, its wear rate was 0.55×10^{-4} $mm^3{\cdot}N^{-1}{\cdot}m^{-1}$, decreased by 59.6% compared to the bare $Ti_{13}Nb_{13}Zr$ alloy.

Microscopic examinations of wear tracks formed on the untreated and carburized samples during linear reciprocating wear tests were conducted and the typical wear morphologies of tested surfaces are displayed in Fig. 10. It was obvious that the bare $Ti_{13}Nb_{13}Zr$ alloy sample suffered severer wear with serious plastic deformation compared to the carburized samples, which coincided with the high wear rate. The emergence of the orientation-ordered ridges and grooves (Fig. 10(a)) parallel to the sliding direction was considered to be the result of plowing and scratching of abrasive particles. In addition, some wear particles removed by spalling were found at some locations on the worn surface, which further revealed that the abrasive wear played a dominant role for bare $Ti_{13}Nb_{13}Zr$ alloy sliding against zirconia ball under the lubrication of calf serum diluted fluid [33, 34]. With respect to the carburized samples, the morphologies of wear tracks were divided into two distinct types. It can be observed that the ETSC0 (Fig. 10(b)) and ETSC10 (Fig. 10(c)) samples with thin and discontinuous TiC layers exhibited coarse worn surface distinguished by delamination pits of large areas and plastic deformation because of the destruction of some relatively soft regions that have not yet finished the conversion to hard TiC [35]. In contrast, the samples (Figs. 10(d)–10(f)) subjected longer holding time (≥30 min) only showed a bit of dispersive adhesive craters rather than severe delamination due to the efficient protection by the thicker TiC ceramic layer [36]. Therefore, the

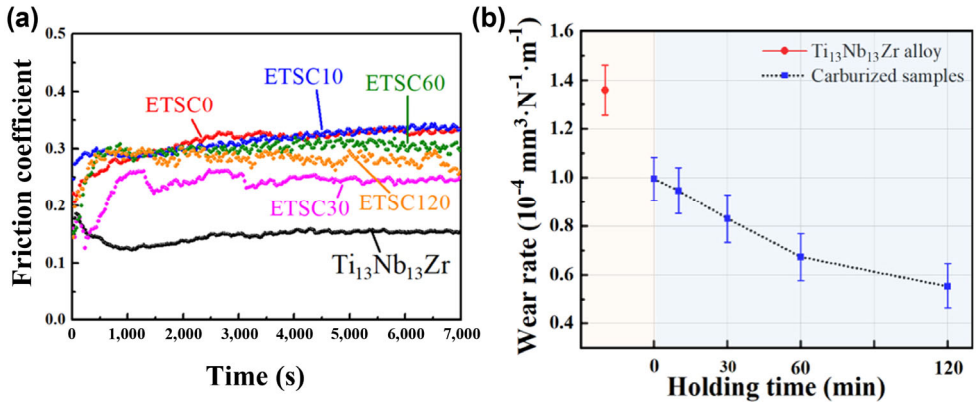

Fig. 9 (a) Friction coefficient and (b) wear rate of $Ti_{13}Nb_{13}Zr$ alloy and the carburized samples under bovine serum lubrication.

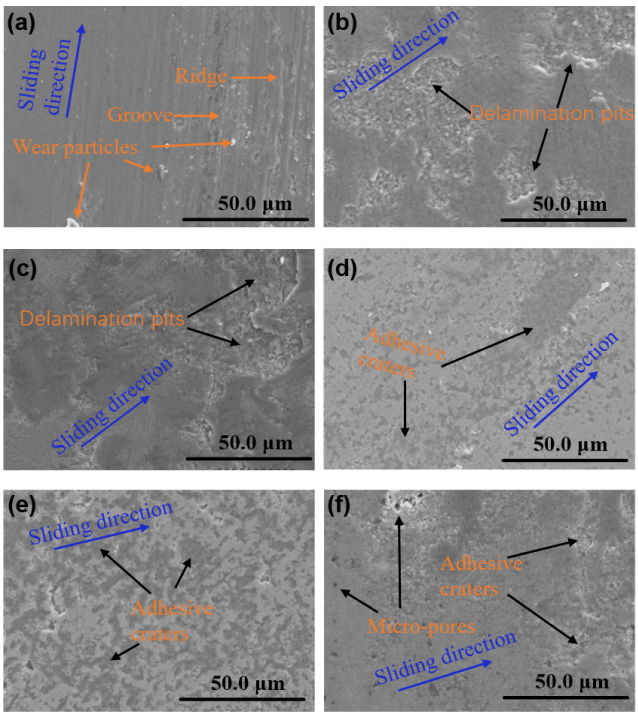

Fig. 10 Typical wear morphologies of the wear tracks formed under bovine serum lubrication on (a) $Ti_{13}Nb_{13}Zr$ alloy; (b) ETSC0; (c) ETSC10; (d) ETSC30; (e) ETSC60; and (f) ETSC120.

dominant wear mechanism of these samples was mild adhesive wear as evidenced by the presence of adhesive junctions [37]. In addition, it was found that the morphologies of wear tracks of ETSC30 (Fig. 10(d)), 60 (Fig. 10(e)), and 120 (Fig. 10(f)) exhibited similar features under the same wear condition. However, the extent of wear became lighter with the increased holding time due to the formation of the thicker and harder TiC layer. In particular, the wear scar of ESTC120 sample was hardly observed, and there were only a few slight adhesive craters. The unique porous structure of titanium cermet even remained until the finish of wear test. And the morphology analysis revealed that zirconia ball had almost no wear mark after sliding against titanium cermet, indicating excellent wear behavior of titanium cermet/zirconia counterparts. With regard to the wear reduction, the effect of calf serum diluted fluid should also be taken into account [27]. On one hand, the surface micro-pores structure of titanium cermet was conducive to generate the reversed press force under lubrication leading to the decreasing contact area between friction pairs. On the other hand, the protein in the calf serum solution might form a boundary lubrication layer through the adhesion to the porous surface, which significantly reduced the abrasive wear [38–40].

4 Conclusions

In order to explore the growth mechanism of titanium cermet, the elevated temperature solid carburization with varied holding time was employed for $Ti_{13}Nb_{13}Zr$ alloy. Also, the tribological performances of titanium cermet were evaluated through linear reciprocating sliding tests. The following conclusions can be drawn:

1) TiC ceramic layer with micro-pores structure was successfully fabricated on surface of $Ti_{13}Nb_{13}Zr$ alloy. As the holding time increased, the overall thickness of carburized region involving TiC ceramic layer and carbon diffusion zone reached to 100 μm, and the surface hardness increased to 758 HV, approximately four times higher than that of the reference sample.

2) For the growth mechanism of TiC ceramic layer,

when the ambient temperature rose to a certain degree, carbonaceous gas decomposes from carburizer and then converted to free atomic carbons through reduction reaction. With prolonging the holding time, the outer TiC ceramic layer and the inner carbon diffusion zone grew inwards simultaneously due to the synchronization of chemical reaction and physical diffusion of carbon, finally forming a gradient carbon distribution.

3) Compared with bare $Ti_{13}Nb_{13}Zr$ alloy, titanium cermet showed increased friction coefficient but significantly reduced wear rate when sliding against zirconia ball under calf serum lubrication condition because of the formation of the hard TiC ceramic layer. Especially, the wear rate of the titanium cermet sample subjected to 120 min carburization at 1,500 K decreased by 59.6% compared to $Ti_{13}Nb_{13}Zr$ alloy. An evolution of wear mechanism from severe abrasive wear for $Ti_{13}Nb_{13}Zr$ alloy to mild adhesive wear for titanium cermet occurred, and the wear extent of titanium cermet became light with the increased holding time under the same wear condition.

Acknowledgements

This work was supported by National Natural Science Foundation of China (Nos. 51875563, 51575514, and 51911530200), and the Tribology Science Fund of State Key Laboratory of Tribology (No. SKLTKF19A03).

References

[1] Zhan C, Kaczmarek R, Loyo-Berrios N, Sangl J, Bright R A. Incidence and short-term outcomes of primary and revision hip replacement in the United States. *J Bone Jt Surg Am Vol* **89**: 526–533 (2007)

[2] Prendki V, Zeller V, Passeron D, Desplaces N, Mamoudy P, Stirnemann J, Marmor S, Ziza J M. Outcome of patients over 80 years of age on prolonged suppressive antibiotic therapy for at least 6 months for prosthetic joint infection. *Int J Infect Dis* **29**: 184–189 (2014)

[3] López G D. Biodeterioration and corrosion of metallic implants and prostheses. *Medicina* **53**: 260–274 (1993)

[4] Maya S, Prakash T, Madhu K D, Goli D. Multifaceted effects of aluminium in neurodegenerative diseases: A review. *Biomed Pharmacother* **83**: 746–754 (2016)

[5] Geetha M, Singh A K, Asokamani R, Gogia A K. Ti based biomaterials, the ultimate choice for orthopaedic implants - A review. *Prog Mater Sci* **54**: 397–425 (2009)

[6] Tekin K C, Malayoglu U, Shrestha S. Tribological behaviour of plasma electrolytic oxide coatings on Ti6Al4V and cp-Ti alloys. *Surf Eng* **32**: 435–442 (2016)

[7] Ossowska A, Beutner R, Scharnweber D, Zielinski A. Properties of composite oxide layers on the $Ti_{13}Nb_{13}Zr$ alloy. *Surf Eng* **33**: 841–848 (2017)

[8] Khan M S, Li Z, Yang K, Xu D K, Yang C, Liu D, Lekbach Y, Zhou E Z, Kalnaowakul P. Microbiologically influenced corrosion of titanium caused by aerobic marine bacterium Pseudomonas aeruginosa. *J Mater Sci Technol* **35**: 216–222 (2019)

[9] Luo Y. Ge S. Jin Z. Fisher J. Formation of titanium carbide coating with micro-porous structure. *Appl Phys A: Mater Sci Process* **98**: 765–768 (2009)

[10] Luo Y, Ge S, Liu H, Jin Z. Microstructure analysis and wear behavior of titanium cermet femoral head with hard TiC layer. *J Biomech* **42**: 2708–2711 (2009)

[11] Luo Y, Jiang H, Cheng G, Liu H. Effect of carburization on the mechanical properties of biomedical grade titanium alloys. *Journal of Bionic Engineering* **8**: 86–89 (2011)

[12] Luo Y, Ge S, Jin Z. Wettability modification for biosurface of titanium alloy by means of sequential carburization. *J Bionic Eng* **6**: 219–223 (2009)

[13] Hanawa T. Metal ion release from metal implants. *Mater Sci Eng C* **24**: 745–752 (2004)

[14] Li J, Zhao Y. Biocompatibility and antibacterial performance of titanium by surface treatment. *J Coat Technol Res* **9**: 223–228 (2009)

[15] Mohan L, Anandan C. Wear and corrosion behavior of oxygen implanted biomedical titanium alloy Ti–13Nb–13Zr. *Appl Surf Sci* **282**: 281–290 (2013)

[16] Pérez D A G, Jorge Junior A M, Asato G H, Lepretre J, Roche V, Bolfarini C, Botta W J. Surface anodization of the biphasic $Ti_{13}Nb_{13}Zr$ biocompatible alloy: Influence of phases on the formation of TiO_2 nanostructures. *J Alloys Compd* **796**: 93–102 (2019)

[17] Yang C C, Ding S J, Lin T H, Yan M. Mechanical and optical properties evaluation of rapid sintered dental zirconia. *Ceram Int* **46**: 26668–26674 (2020)

[18] Durov A V, Naidich Y V, Kostyuk B D. Investigation of interaction of metal melts and zirconia. *J Mater Sci* **40**: 2173–2178 (2005)

[19] Mattei L, Puccio F D, Piccigallo B, Ciulli E. Lubrication and wear modelling of artificial hip joints: A review. *Tribol Int* **44**: 532–549 (2011)

[20] Mavraki A, Cann P M. Lubricating film thickness measurements with bovine serum. *Tribol Int* **44**: 550–556 (2011).

[21] Zhao Z, Hui P, Wang T, Wang X, Xu Y, Zhong L, Zhao M. New strategy to grow TiC coatings on titanium alloy: Contact solid carburization by cast iron. *J Alloys Compd* **745**: 637–643 (2018)

[22] Lu W J, Zhang D, Zhang X N, Wu R J, Sakata T, Mori H. Microstructural characterization of TiB in *in situ* synthesized titanium matrix composites prepared by common casting technique. *J Alloys Compd* **327**: 240–247 (2001)

[23] Redmore E, Li X, Dong H. Tribological performance of surface engineered low-cost beta titanium alloy. *Wear* **426–427**: 952–960 (2019)

[24] Duan H, Han Y, LÜ W, Mao J, Wang L, Zhang D. Effect of solid carburization on surface microstructure and hardness of Ti–6Al–4V alloy and $(TiB+La_2O_3)$/Ti–6Al–4V composite. *Trans Nonferrous Met Soc China* **26**: 1871–1877 (2016)

[25] Coelho P G, Jimbo R, Tovar N, Bonfante E A. Osseointegration: Hierarchical designing encompassing the macrometer, micrometer, and nanometer length scales. *Dental Materials Official Publication of the Academy of Dental Materials* **31**: 37–52 (2015)

[26] Nadezhdin S V, Zubareva E V, Burda Y E, Kolobov Y R, Ivanov M B, Khramov G V, Afanas'Ev A Y. Influence of Implants Surface Properties on Bone Tissue Formation in the Ectopic Osteogenesis Test. *Bull Exp Biol Med* **162**: 812–814 (2017)

[27] Wang K, Xiong D. Construction of lubricant composite coating on Ti_6Al_4V alloy using micro-arc oxidation and grafting hydrophilic polymer. *Mater Sci Eng C Mater Biol Appl* **90**: 219–226 (2018)

[28] Vajpai S K, Sharma B, Ota M, Ameyama K. Effect of cold rolling and heat-treatment on the microstructure and mechanical properties of β-titanium Ti–25Nb–25Zr alloy. *Mater Sci Eng A* **736**: 323–328 (2018)

[29] Chen Y, Yang C, Fan C, Zhuo Y, Lin S, Chen C. Microstructure evolution mechanism and mechanical properties of TC11–TC17 dual alloy after annealing treatment. *J Alloys Comp* **842**: 155874 (2020)

[30] Cheng K, Pagan N, Bijukumar D, Mathew M T, McNallan M. Carburized titanium as a solid lubricant on hip implants: Corrosion, tribocorrosion and biocompatibility aspects. *Thin Solid Films* **665**: 148–158 (2018)

[31] Essa F A, Zhang Q, Huang X, Ibrahim A M M, Ali M K A, Sharshir S W. Enhancing the tribological and mechanical properties of M50 steel using solid lubricants- A detailed review. *Proc Inst Mech Eng, Part J* **232**: 619–642 (2017)

[32] Guo L, Qin L, Kong F, Yi H, Tang B. Improving tribological properties of Ti–5Zr–3Sn–5Mo–15Nb alloy by double glow plasma surface alloying. *Appl Surf Sci* **388**: 203–211 (2016)

[33] Mehdi M, Farokhzadeh K, Edrisy A. Dry sliding wear behavior of superelastic Ti–10V–2Fe–3Al β-titanium alloy. *Wear* **350–351**: 10–20 (2016)

[34] Essa F A, Zhang Q, Huang X, Ali M K A, Elagouz A, Abdelkareem M A A. Effects of ZnO and MoS_2 solid lubricants on mechanical and tribological properties of M50-steel-based composites at high temperatures: Experimental and simulation study. *Tribol Lett* **65**: 97 (2017)

[35] Essa F A, Zhang Q, Huang X. Investigation of the effects of mixtures of WS_2 and ZnO solid lubricants on the sliding friction and wear of M50 steel against silicon nitride at elevated temperatures. *Wear* **374–375**: 128–141 (2017)

[36] Ye J, Xiong J, Guo Z, Yang T, Zhou L, Liu J, Li S, Li T. Preparation of self-lubricating Ti(C,N)-based cermets by solid carburization and wear behavior. *Int J Refract Hard Met* **67**: 68–73 (2017)

[37] Essa F A, Zhang Q, Huang X, Ibrahim A M M, Ali M K A, Abdelkareem M A A, Elagouz A. Improved friction and wear of M50 steel composites incorporated with ZnO as a solid lubricant with different concentrations under different loads. *J Mater Eng Perform* **26**: 4855–4866 (2017)

[38] Heuberger M P, Widmer M R, Zobeley E, Glockshuber R, Spencer N D. Protein-mediated boundary lubrication in arthroplasty. *Biomaterials* **26**: 1165–1173 (2005)

[39] Sawae Y, Yamamoto A, Murakami T. Influence of protein and lipid concentration of the test lubricant on the wear of ultra high molecular weight polyethylene. *Tribol Int* **41**: 648–656 (2008)

[40] Myant C, Underwood R, Fan J, Cann P M. Lubrication of metal-on-metal hip joints: the effect of protein content and load on film formation and wear. *J Mech Behav Biomed Mater* **6**: 30–40 (2012)

Xiaolei SUN. He received his bachelor degree in material forming and control engineering in 2017 from Hubei University of Automotive Technology, Hubei, China. At present, he is studying for his doctorate in mineral materials engineering at China University of Mining and Technology, Jiangsu, China. His research interests include biomaterials and tribology.

Yong LUO. He received his Ph.D. in mechanical engineering from the China University of Mining and Technology in 2008. Currently, he is a professor and Ph.D. supervisor in the School of Materials Science and Physics, China University of Mining and Technology. His research area covers artificial joints, biotribology, surface and interface sciences, and biomaterials.